Research in Astronomy and Astrophysics, 22:125006 (13pp), 2022 December https://doi.org/10.1088/1674-4527/ac9780

The Dependence of Stellar Activity Cycles on Effective Temperature

Leonid Kitchatinov
Institute of Solar-Terrestrial Physics SB RAS, Lermontov Str. 126A, Irkutsk 664033, Russia; kit@iszf.irk.ru
Received 2022 May 13; revised 2022 September 22; accepted 2022 September 30; published 2022 November 11

Abstract

This paper proposes the idea that the observed dependence of stellar activity cycles on rotation rate can be a manifestation of a stronger dependence on the effective temperature. Observational evidence is recalled and theoretical arguments are given for the presence of cyclic activity in the case of sufficiently slow rotation only. Slow rotation means proximity to the observed upper bound on the rotation period of solar-type stars. This maximum rotation period depends on temperature and shortens for hotter stars. The maximum rotation period is interpreted as the minimum rotation rate for operation of a large-scale dynamo. A combined model for differential rotation and the dynamo is applied to stars of different mass rotating with a rate slightly above the threshold rate for the dynamo. Computations show shorter dynamo cycles for hotter stars. As the hotter stars rotate faster, the computed cycles are also shorter for faster rotation. The observed smaller upper bound for rotation period of hotter stars can be explained by the larger threshold amplitude of the α-effect for onset of their dynamos: a larger α demands faster rotation. The amplitude of the (cycling) magnetic energy in the computations is proportional to the difference between the rotation period and its upper bound for the dynamo. Stars with moderately different rotation rates can differ significantly in super-criticality of their dynamos and therefore in their magnetic activity, as observed.

Key words: dynamo – stars: activity – stars: magnetic field – stars: solar-type – stars: rotation

1. Introduction

Large-scale magnetic fields and large-scale flows in late-type stars are believed to be caused by global rotation. Accordingly, many observational and theoretical studies are focused on the dependence of stellar magnetic activity and/or differential rotation on the rotation rate. This paper suggests that magnetic activity *cycles* and differential rotation are more sensitive to another stellar parameter of the effective temperature.

The temperature dependence can manifest itself as seeming dependence on rotation rate because of the following. Solar-type stars are spinning-down with age due to the angular momentum loss for magnetically coupled wind (Kraft 1967). Proportionality constant in the Skumanich (1972) law $P_{\rm rot}\propto t^{1/2}$ for stellar spindown is a decreasing function of temperature (Barnes 2007). Among stars of approximately the same age t, cooler stars have longer rotation period $P_{\rm rot}$. Relatively fast rotation in a sample of (solar-type) stars is usually represented by F-stars while cooler K-stars are on the slow rotation side of the sample (see Figure 3 in Donahue et al. 1996, as a characteristic example). A rotation rate dependence inferred from the sample can therefore include an implicit dependence on temperature.

In the case of differential rotation, this statement is more or less evident by now. Observations (Donati & Collier Cameron 1997; Barnes et al. 2005; Balona & Abedigamba 2016) and theoretical modeling (Kitchatinov & Rüdiger 1999; Kitchatinov & Olemskoy 2012) both suggest that former detections of an increasing trend in dependence of the differential rotation on rotation rate can result from combining a strong increase of the differential rotation with temperature with its moderate dependence on rotation rate.

This paper considers the possibility that stellar activity cycles can also be more dependent on temperature than on the rate of rotation. Observations of stellar cycles were mainly focused on the dependence on rotation rate. A tendency of shorter cycles for faster rotation has been found (Noyes et al. 1984b) though with a considerable scatter and possible discontinuities in this trend (Brandenburg et al. 1998; Saar & Brandenburg 1999; Böhm-Vitense 2007). Several attempts at reproducing the trend with dynamo models were undertaken with mixed success (Jouve et al. 2010; Karak et al. 2014; Hazra et al. 2019; Pipin 2021). There is an extensive literature on direct numerical simulations of global stellar convection including simulations of the activity cycles (see Strugarek et al. 2017, 2018; Warnecke 2018; Brun et al. 2022, and references therein). The decreasing trend in cycle duration with rotation rate remains however unexplained.

Observations of stellar rotation revealed the upper bound on rotation period of solar-type stars (Rengarajan 1984; van Saders et al. 2016). Magnetic activity is low near this maximum rotation period (Metcalfe et al. 2016). The maximum period can therefore be interpreted as a minimum rotation rate for large-scale stellar dynamos (Kitchatinov & Nepomnyashchikh 2017b; Cameron & Schüssler 2017; Metcalfe & Egeland 2019). We keep to this interpretation and apply a joint mean-field

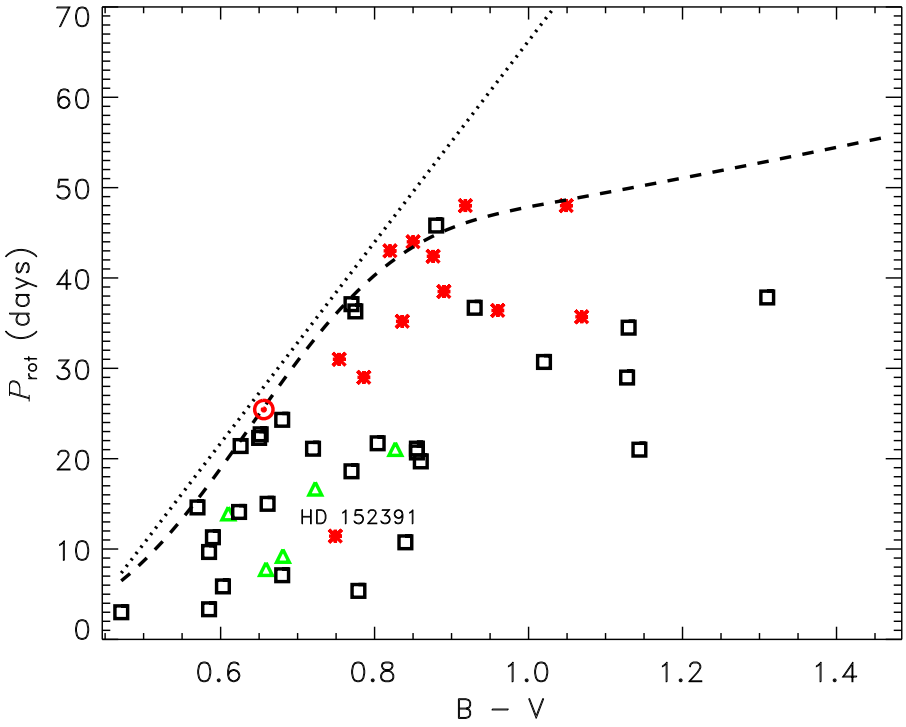

Figure 1. Positions of the main sequence stars showing activity cycles on the P_{rot}–$(B-V)$ plane. Red symbols correspond to stars with well-defined solar-like activity cycles. Green triangles signify stars with multiple cycles and black squares—the stars with uncertain "probable" cycles. The dotted and dashed lines represent the maximum rotation period P_{max} for stellar spindown according to Rengarajan (1984) and van Saders et al. (2019) respectively.

model for differential rotation and dynamo to stars of different mass rotating with a period close to its observationally detected upper bound. The computations show an increase in differential rotation and shortening of the dynamo-cycle for stars of higher mass and effective temperature. As the maximum rotation period is shorter for hotter stars (van Saders et al. 2019), the temperature trends also imply shorter cycles and larger differential rotation for faster rotation, though the rotation rate is not the main physical parameter governing the trends.

We also recall observational evidence and discuss theoretical arguments for the presence of activity cycles in sufficiently slowly rotating stars only. This is done in the following Section 2. Section 3 explains our method and the dynamo model. Section 4 presents and discusses the results. Section 5 summarizes the results and concludes.

2. Should Cyclic Activity be Expected for Rapid Rotators?

The project of long-term monitoring of chromospheric activity at the Mount Wilson Observatory revealed activity cycles similar to the 11 yr solar cycle on many Sun-like stars (Wilson 1978; Baliunas et al. 1995). Summarizing the results of the project, Baliunas et al. (1995) noted that cycles on young rapid rotators are rare but slow rotators as old as the Sun have cycles (except for the cases of flat and low activity like the solar Maunder minimum). Recently, Boro Saikia et al. (2018) compiled a chromospheric activity catalog of Mount Wilson data and more recent data on solar-type stars. Their Table 4 gives stars with cyclic activity.

Figure 1 shows positions of the stars with activity cycles from the catalog by Boro Saikia et al. (2018) on the plane of the rotation period P_{rot} and the $B-V$ color. Only main sequence stars are included in the plot.[1]

Figure 1 displays also the observed upper bound P_{max} on the rotation period. The dotted line in Figure 1 is the linear approximation for the P_{max}–$(B-V)$ relation by Rengarajan (1984). Rengarajan found this approximation for $B-V<1$. Based on vast statistics from recent data on stellar rotation, van Saders et al. (2019) found that the P_{max}–$(B-V)$ relation is well approximated by the constant value

$$\mathrm{Ro} = 2.08, \tag{1}$$

of the Rossby number $\mathrm{Ro} = P_{rot}/\tau_c$; the convective turnover time τ_c is a function of $B-V$ color (see Equation (4) in Noyes et al. 1984a). The P_{max} after Equation (1) is represented by the

[1] Some inaccuracies were corrected in Table 4 by Boro Saikia et al. (2018) when producing Figure 1: The color $B-V=0.594$ given in the table for HD 160343 is too small for the K3 star. It was corrected to the value of 0.971 observed (Høg et al. 2000). HD 81809 misclassified in the table as a main sequence star is a binary system whose active component is subgiant (Egeland 2018). Subgiants are not included in Figure 1.

dashed line in Figure 1. Proximity to this line can quantify the meaning of "slow rotation" for the main sequence dwarfs.

Following Boro Saikia et al. (2018), the quality of the activity cycles in Figure 1 is encoded by color: red symbols correspond to well defined solar-like cycles, green triangles mark stars with multiple cycles and black squares—stars with "probable" cycles. Almost all stars with well-defined cycles are slow rotators with $P_{\rm rot}$ close to $P_{\rm max}$. The only exception is HD 152391. Olspert et al. (2018) found doubly periodic activity for this star with their harmonic regression model. This may explain the position of HD 152391 in the region of green symbols in Figure 1.

Also on physical grounds, it seems plausible to expect cyclic activity for slow rotators only.

Hydromagnetic dynamos of any kind can be understood as the *instability* of conducting fluids to magnetic disturbances: only if whatever small but finite seed field is present can a dynamo-instability amplify and support the field. Similar to all other instabilities, dynamo-instability has dimensionless governing parameters and onset when the parameters exceed a certain threshold value. The empirical Equation (1) can be seen as the normalized rotation rate for the onset of large-scale stellar dynamos. The red symbols in Figure 1 close to the $P_{\rm max}$-line represent slightly supercritical cyclic dynamos.

Various instabilities behave similarly in dependence on their governing parameters. For slightly supercritical parameters, new steady (change of stability) or oscillatory (overstability) states are normally realized (Chandrasekhar 1961). In a highly supercritical case, instabilities change—as a rule—to a turbulent regime possibly with an intermediate stage of multi-periodic dynamics (see, e.g., Landau & Lifshitz 1987). If large-scale dynamo instability is not an exception to this rule, some kind of dynamo turbulence with non-cyclic activity should be expected for the highly supercritical regime of rapid rotation.

The expectation is hard to test with computations. This would require fully nonlinear and highly supercritical dynamo models lacking at the moment. The strongly nonlinear regime of dynamos in rapid rotators is in particular indicated by their observed large torsional oscillations (Collier Cameron & Donati 2002). Changes to turbulence usually proceed via break of symmetry of slightly supercritical regimes. An adequate dynamo model has to be nonlinear and non-axisymmetric.

Lacking such a dynamo model, computations for this paper are restricted to slightly supercritical cyclic dynamos of stars with rotation period close to $P_{\rm max}$ of Figure 1 corresponding to the constant Rossby number of Equation (1).

3. Model and Method

3.1. Combined Model of Differential Rotation and Dynamo

We apply a joint model of dynamo and differential rotation by Kitchatinov & Nepomnyashchikh (2017a, 2017b) to stars of different mass $0.7 \leqslant M/M_\odot \leqslant 1.2$ and rotation period close to $P_{\rm max}$ of Equation (1). Differential rotation and meridional flow for dynamo computations are supplied by an axisymmetric hydrodynamical mean-field model. The model differs from that of Kitchatinov & Olemskoy (2011) only in a modification of the mixing length ℓ: the mixing length of its standard definition $\ell_0 = \alpha_{\rm MLT} {\rm H_p}$ ($\rm H_p$ is the pressure scale height) is now reduced near the inner boundary $r_{\rm i}$ of the convection zone so that it can exceed the distance to the boundary only slightly

$$\ell = \ell_{\rm min} + \frac{1}{2}(\ell_0 - \ell_{\rm min})\left[1 + {\rm erf}\left(\frac{r/r_{\rm i} - x_\ell}{d}\right)\right]. \qquad (2)$$

In this equation, $\ell_{\rm min} = 0.01R$ equals one percent of the stellar radius, erf is the error function and other parameters will be specified later. Our differential rotation model differs from other mean-field formulations in that it does not prescribe the eddy transport coefficients but computes them. The eddy viscosity in particular is defined by the equation

$$\nu_{\rm T} = -\frac{\tau \ell g}{15 c_{\rm p}} \frac{\partial S}{\partial r}, \qquad (3)$$

where g is gravity, τ is the (position dependent) convective turnover time and $c_{\rm p}$ is the specific heat capacity at constant pressure. The specific entropy S in Equation (3) is a dependent variable of the model. The entropy is controlled by the (nonlinear) heat transport equation that is one of three equations in the model (with the other two being the equations for the meridional flow and angular velocity). Recently Jermyn et al. (2018) discussed the performance of this closure method in the convective turbulence theory.

We avoid repeating other details of the differential rotation model, all of which can be found elsewhere (Kitchatinov & Olemskoy 2011, 2012).

Our dynamo model is a particular version of the flux-transport models pioneered by Choudhuri et al. (1995) and Durney (1995). The models' name reflects the importance of magnetic field advection by the meridional flow. The flux-transport models with the α-effect of Babcock–Leighton (BL) type agree closely with solar observations (Jiang et al. 2013; Charbonneau 2020).

Our dynamo model is formulated for a spherical layer of a stellar convection zone. The standard spherical coordinate system (r, θ, ϕ) with the rotation axis as the polar axis is used. The formulation assumes axial symmetry of the mean magnetic field

$$\boldsymbol{B} = \hat{\phi} B + \boldsymbol{\nabla} \times \left(\hat{\phi} \frac{A}{r \sin\theta}\right), \qquad (4)$$

and flow

$$\boldsymbol{V} = \hat{\phi}\, r \sin\theta\, \Omega + \rho^{-1} \boldsymbol{\nabla} \times \left(\hat{\phi} \frac{\psi}{r \sin\theta}\right). \qquad (5)$$

In these equations, B is the toroidal magnetic field, A is the poloidal field potential, Ω is the angular velocity, ψ is the stream function for the meridional flow, $\hat{\phi}$ is the azimuthal unit vector and ρ is density.

Two joint dynamo equations for the poloidal and toroidal magnetic fields read

$$\frac{\partial A}{\partial t}=\frac{1}{\rho r^2\sin\theta}\left(\frac{\partial\psi}{\partial r}\frac{\partial A}{\partial\theta}-\frac{\partial\psi}{\partial\theta}\frac{\partial A}{\partial r}\right)+r\sin\theta\,\mathcal{E}_\phi, \tag{6}$$

$$\frac{\partial B}{\partial t}=\frac{1}{\rho r^2}\frac{\partial\psi}{\partial r}\frac{\partial}{\partial\theta}\left(\frac{B}{\sin\theta}\right)-\frac{1}{r\sin\theta}\frac{\partial\psi}{\partial\theta}\frac{\partial}{\partial r}\left(\frac{B}{\rho r}\right)+\frac{1}{r}\left(\frac{\partial\Omega}{\partial r}\frac{\partial A}{\partial\theta}-\frac{\partial\Omega}{\partial\theta}\frac{\partial A}{\partial r}+\frac{\partial(r\mathcal{E}_\theta)}{\partial r}-\frac{\partial\mathcal{E}_r}{\partial\theta}\right), \tag{7}$$

where $\boldsymbol{\mathcal{E}}=\langle\boldsymbol{u}\times\boldsymbol{b}\rangle$ is the mean electromotive force (EMF, Krause & Rädler 1980), which results from a correlated action of fluctuating velocities $\boldsymbol{u}$ and magnetic fields $\boldsymbol{b}$ and includes all the dynamo-relevant effects of convective turbulence.

Expression for the EMF can be rather complicated (Pipin 2008). Some simplification can be achieved by splitting the EMF into three parts,

$$\boldsymbol{\mathcal{E}}=\boldsymbol{\mathcal{E}}^{\alpha}+\boldsymbol{\mathcal{E}}^{\rm diff}+\boldsymbol{\mathcal{E}}^{\rm dia}, \tag{8}$$

responsible for the α-effect, eddy diffusion and diamagnetic pumping respectively.

Toroidal field generation by the α-effect is neglected in the $\alpha\Omega$-dynamo. Nonlocal α-effect of BL type is prescribed in the poloidal field Equation (6)

$$\mathcal{E}^{\alpha}_{\phi}=\frac{\alpha\,B(r_{\rm i},\,\theta)}{1+(B(r_{\rm i},\,\theta)/B_0)^2}\cos\theta\sin^{n_\alpha}\theta\;\phi_\alpha(r/r_{\rm e}), \tag{9}$$

where the function

$$\phi_\alpha(r/r_{\rm e})=\frac{1}{2}[1+{\rm erf}((r/r_{\rm e}+2.5h_\alpha-1)/h_\alpha)], \tag{10}$$

with $h_\alpha=0.02$ peaking near the external boundary $r_{\rm e}=0.97R$. This boundary is placed slightly below the stellar surface to exclude the near-surface layer with steep stratification that is difficult to include in the differential rotation model. The α-effect of Equation (9) describes generation of the poloidal field near the surface from the bottom toroidal field. The large value of $n_\alpha=7$ used in the model implies that the magnetic flux-tubes whose rise to the surface produces the α-effect are formed at low latitudes (Kitchatinov 2020). The value $B_0=10^4$ G of the α-effect quenching parameter in Equation (9) gives reasonable results for the Sun (Kitchatinov & Nepomnyashchikh 2017a). This value was used for the star of one solar mass. For other masses, the parameter was re-scaled in proportion to the square root of density at the inner boundary, $B_0=10^4\sqrt{\rho_{\rm i}(M)/\rho_i(1M_\odot)}$ G, to reflect the scaling of flux-tube rise velocity with the Alfvén velocity (D'Silva & Choudhuri 1993).

Diffusive part of the EMF of our model reads

$$\boldsymbol{\mathcal{E}}^{\rm diff}=-\eta\boldsymbol{\nabla}\times\boldsymbol{B}-\eta_\parallel\hat{\boldsymbol{\Omega}}\times(\hat{\boldsymbol{\Omega}}\cdot\boldsymbol{\nabla})\boldsymbol{B}, \tag{11}$$

where $\hat{\boldsymbol{\Omega}}=\boldsymbol{\Omega}/\Omega$ is the unit vector along the rotation axis. Magnetic diffusivity of Equation (11) is anisotropic: the diffusivity η for a direction normal to the rotation axis is smaller than the diffusivity $\eta+\eta_\parallel$ along this axis. The anisotropy is caused by rotation,

$$\eta=\eta_{\rm T}\phi(\Omega^*),\quad \eta_\parallel=\eta_{\rm T}\phi_\parallel(\Omega^*). \tag{12}$$

The functions $\phi(\Omega^*)$ and $\phi_\parallel(\Omega^*)$ of the Coriolis number

$$\Omega^*=2\tau\Omega, \tag{13}$$

are given in Kitchatinov et al. (1994). The rotationally induced anisotropy is important for the differential rotation model. Only by accounting for anisotropy of the eddy heat transport can the helioseismological rotation law be reproduced (Rüdiger et al. 2013). We include the diffusion anisotropy in the dynamo model for consistency and for its better performance (Pipin et al. 2012).

The diamagnetic pumping results from inhomogeneity of the turbulence intensity (Krause & Rädler 1980). Our dynamo model employs the anisotropic pumping effect for rotating fluids as it was derived by Kitchatinov & Nepomnyashchikh (2016),

$$\boldsymbol{\mathcal{E}}^{\rm dia}=-(\boldsymbol{\nabla}\tilde{\eta})\times\boldsymbol{B}+(\boldsymbol{\nabla}\eta_\parallel)\times\hat{\boldsymbol{\Omega}}(\hat{\boldsymbol{\Omega}}\cdot\boldsymbol{B}), \tag{14}$$

with another diffusivity coefficient

$$\tilde{\eta}=\eta_{\rm T}\phi_1(\Omega^*). \tag{15}$$

Allowance for the pumping effect generally improves performance of the solar dynamo models (Guerrero & Pino 2008; Karak & Cameron 2016; Zhang & Jiang 2022).

Magnetic eddy diffusivity $\eta_{\rm T}$ can be estimated using the computed eddy viscosity of Equation (3), $\eta_{\rm T}=\nu_{\rm T}/{\rm Pm}$, where Pm is the magnetic Prandtl number. The problem however is that our differential rotation model uses local mixing-length approximation and does not include the low diffusivity layer of overshoot convection that is important for the dynamo. We reduce the diffusivity near the inner boundary to model the layer

$$\eta_{\rm T}=\frac{1}{\rm Pm}\left[\nu_{\rm i}+\frac{1}{2}(\nu_{\rm T}-\nu_{\rm i})\left(1+{\rm erf}\left(\frac{r/r_{\rm i}-x_\eta}{d}\right)\right)\right], \tag{16}$$

where $\nu_{\rm i}=10^{-4}\nu_{\rm max}$ ($\nu_{\rm max}$ is the maximum value of $\nu_{\rm T}$ within the convection zone) and Pm=3 in all computations of this paper. Parameters in Equations (2) and (16) for the star of 1 $M_\odot$ are taken to be $x_\ell=1.01$, $d=0.025$ and $x_\eta=1.1$.

Figure 2 plots depth profiles of the diffusivity coefficients of Equations (11) and (15) for the 1 $M_\odot$ star. The large (but realistic, Cameron & Schüssler 2016) diffusivity of this figure can result in too short dynamo-cycles. Cycle periods of about

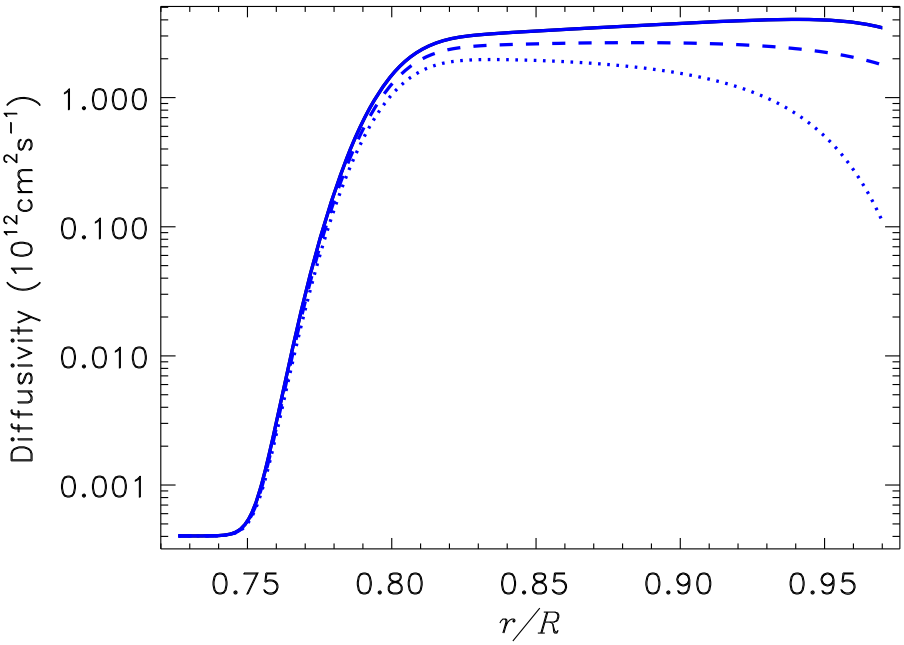

Figure 2. Depth profiles of the diffusion coefficients η (solid line), $\eta_\parallel$ (dotted line) and $\tilde{\eta}$ (dashed line) for a star of 1 $M_\odot$ rotating with a period of 23.5 days.

10 yr in our model are due to the downward diamagnetic pumping that transports the magnetic field into the near-bottom layer with low diffusion.

The $\eta_\parallel$ coefficient decreases toward the surface in Figure 2. This is because the depth-dependent Coriolis number of Equation (13) decreases toward the surface, leading to a smaller diffusion anisotropy induced by rotation.

The parameter values $x_\ell = 1.01$, $d = 0.025$ and $x_\eta = 1.1$ were formerly applied to stars with various masses (Kitchatinov & Nepomnyashchikh 2017b). It has been realized since then that the near bottom layer of small diffusion occupies a larger part of the convection zone in stars with larger mass in this case (half of the thin convection zone of the 1.2 $M_\odot$ star). To avoid such a non-physical prescription, we re-scale the parameters so that all the characteristic scales constitute the same fractions of the convection zone thickness in stars of different mass

$$d = 0.0745\left(\frac{r_\mathrm{e}}{r_\mathrm{i}} - 1\right),$$
$$x_\ell = 0.03\frac{r_\mathrm{e}}{r_\mathrm{i}} + 0.97,\ \ x_\eta = 0.3\frac{r_\mathrm{e}}{r_\mathrm{i}} + 0.7. \qquad (17)$$

With this prescription, Figure 2 looks almost the same for stars of all considered mass except for the varying minimum value of r/R in the plot. Some difference in the results of this paper with Kitchatinov & Nepomnyashchikh (2017b) is explained by the different prescription for the parameters of Equation (17) and in the definition of P_max by Equation (1) which was not yet reported in 2017.

The dynamo model solves numerically the initial value problem for dynamo Equations (7) with a perfect conductor boundary condition imposed on the bottom and vertical field condition on the top. The initial condition prescribes the zero toroidal field and the potential

$$A_0(r,\,\theta) = \frac{B_N(r - r_\mathrm{i})(2r_\mathrm{e} - r_\mathrm{i} - r)}{4(1 - r_\mathrm{i}/r_\mathrm{e})^2} \times [1 - p + (1 + p)\cos\theta]\sin^2\theta, \qquad (18)$$

for the poloidal field, where B_N is the field strength on the northern pole and $-1 \leqslant p \leqslant 1$ is the parity index ($p = 1$ means a quadrupolar equator-symmetric initial field and it is $p = -1$ for a dipolar antisymmetric field). Starting from the initial condition of mixed parity, the dynamo code was run for one-thousand years simulated time. This preliminary run suffices for the dynamo to converge to a periodic oscillation, for which the cycle period and other results of Section 4 were obtained. If the initial condition (18) had a certain parity ($p = \pm 1$), the numerical solution cannot depart from this parity. The runs with so-prescribed parity helped to compute the threshold amplitude α_c of the α-effect of Equation (9) for the onset of dynamo-instability for dipolar ($\alpha_\mathrm{c}^\mathrm{d}$) and quadrupolar ($\alpha_\mathrm{c}^\mathrm{q}$) fields.

3.2. Estimating Rotation Period and Structure of Stars

Computations of differential rotation and dynamo require the structure and rotation rate of a star to be specified.

We use the gyrochronology relation by Barnes (2007)

$$P_\mathrm{rot} = at^n(B - V - 0.4)^b \ \mathrm{day}, \qquad (19)$$

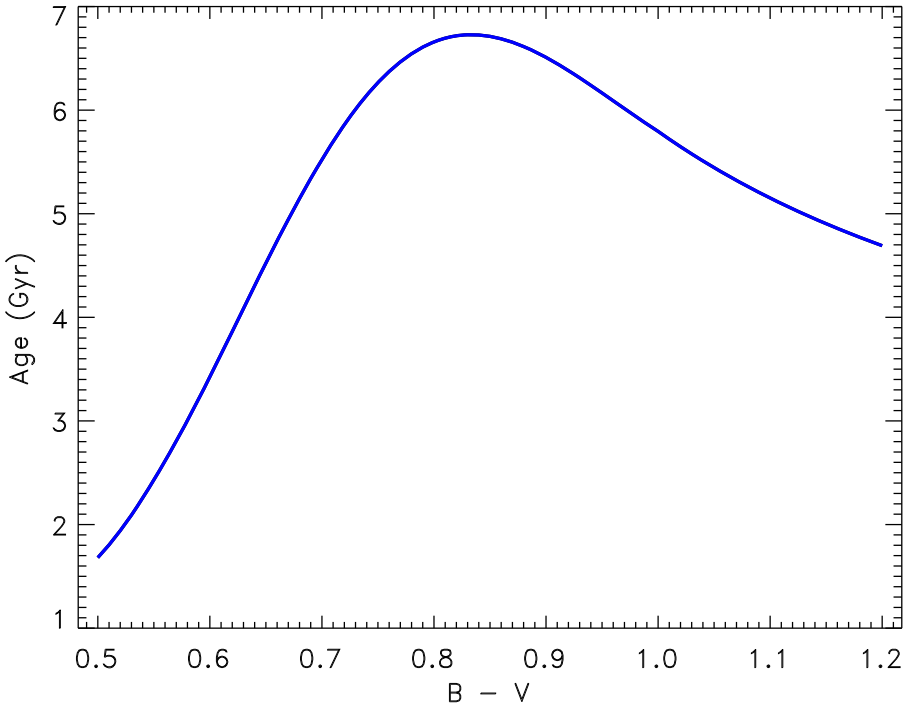

Figure 3. Stellar age of the maximum rotation period $P_{\rm max}$ as a function of $B-V$ color estimated with Equation (20).

relating the age t (in Myr) and $B-V$ color of a star to the rotation period. The parameter values of $a = 0.77$, $n = 0.512$ and $b = 0.6$ within their uncertainty range reproduce closely the case with the Sun.

Gyrochronology is believed to overestimate the rotation period after the rotation slows down to the minimum rate of Equation (1) (van Saders et al. 2016, 2019). Stellar structure varies slowly at the age when it happens. We therefore assume that the relation (19) applies up to the age when the maximum rotation period of Equation (1) is attained. This age can be roughly estimated from the reversed Equation (19)

$$t = \left[\frac{2.08\ \tau_{\rm c}}{a(B-V-0.4)^b}\right]^{1/n}. \qquad (20)$$

Figure 3 displays the age of Equation (20) as a function of $B-V$ color. This age of the large-scale dynamo termination does not decrease monotonically with increasing temperature.

The *EZ* model by Paxton (2004) was used to define the evolutionary sequence of structure models for a star of given mass and metallicity $Z = 0.02$. The color-temperature relation and the interpolation code by VandenBerg & Clem (2003) were used to estimate the $B-V$ color corresponding to the structure models. The rotation period of Equation (19) was then compared with the $P_{\rm max}$ of Equation (1). The structure model with the closest values of these two rotation periods is assumed to correspond to the star that arrived on the dashed line of Figure 1. The Sun is almost on this line. The solar dynamo was estimated to be about 10% supercritical in the sense of the amplitude α of the α-effect of Equation (9) (Kitchatinov & Nepomnyashchikh 2017b). The differential rotation of the stars with different masses which 'arrived on the dashed line' of Figure 1 was computed and then used in the simulations of their 10% supercritical dynamos as explained at the end of Section 3.1.

The computations cover the mass range from 0.7 to 1.2 $M_\odot$ with increment of 0.05 $M_\odot$.

4. Results and Discussion

All computations show solar-type differential rotation with faster equatorial rotation. Figure 4 depicts the surface equator-to-pole difference in rotation rate with dependence on the effective temperature. Hotter stars have larger differential rotation. As the hotter stars rotate faster, this Figure also means an increase in the differential rotation with rotation rate. Figure 4 is a slow rotation counterpart of the observational figure 2 by Barnes et al. (2005) and theoretical figure 10 by Kitchatinov & Olemskoy (2011).

Figure 4 also displays the dimensionless ratio $\Delta\Omega/\Omega$, which varies little with $T_{\rm eff}$. As the computations for this Figure were done for constant ${\rm Ro} = 2.08$, the small variation in $\Delta\Omega/\Omega$ means that $\Delta\Omega\tau_{\rm c}$ also varies little with $T_{\rm eff}$. The increase in $\Delta\Omega$ with $T_{\rm eff}$ proceeds in inverse proportion to decreasing convective turnover time. The scaling with $\tau_{\rm c}^{-1}$ can explain

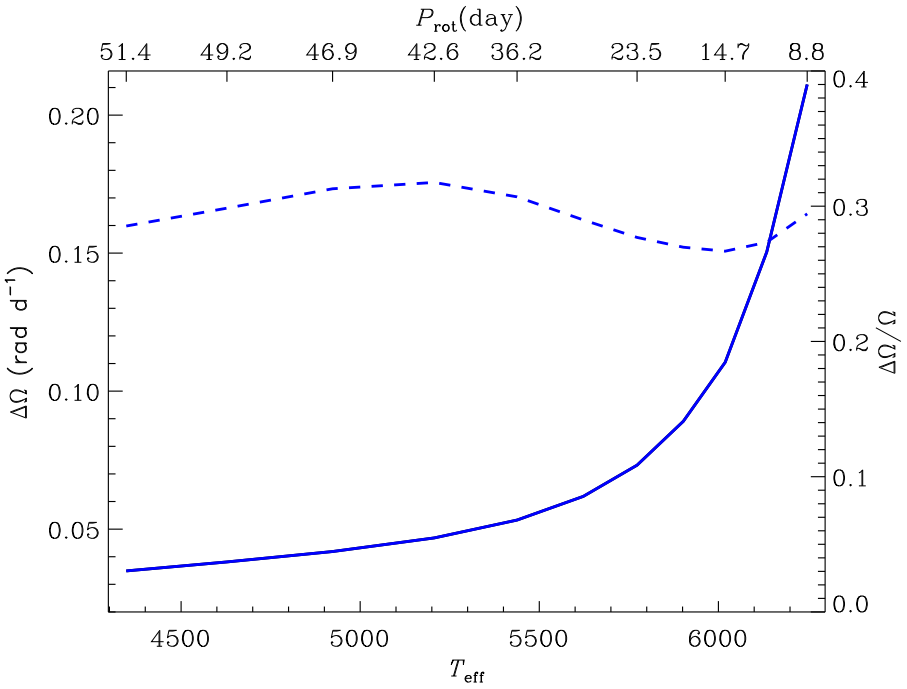

Figure 4. *Solid line, left scale:* difference in rotation rates between equator and pole as a function of temperature. *Dashed line, right scale:* the relative value $\Delta\Omega/\Omega$ of the differential rotation. The scale on the top shows the rotation period corresponding to the dashed line in Figure 1.

the strong increase in differential rotation with temperature observed by Barnes et al. (2005).

Figure 5 features a similar plot for the period of computed dynamo cycles. These are the periods of energy oscillation (half-periods of the sign-changing magnetic cycles). Dynamo computations predict shorter cycles for hotter stars. For fixed Rossby number of Equation (1), this temperature trend also implies a shorter cycle for faster rotation. Similar to the differential rotation, the observed decrease in activity cycle duration with rotation rate can be at least partly explained by its temperature dependence. In difference with the differential rotation, we did not find a normalization for $P_{\rm cyc}$, which varies little with $T_{\rm eff}$.

The difference with the differential rotation also is that the theoretical dependence of cycle period on rotation rate for fixed temperature is uncertain and may not be weak. Non-kinematic dynamo models are required to study this dependence. Consideration of Section 2 suggests that activity of rapidly rotating young stars may not be cyclic. Katsova et al. (2015) estimated that the Sun formed its activity cycle at the age of 1–2 Gyr. This means about two times faster rotation compared to its present rate. Red symbols in Figure 1 are not very close to the dashed line of $P_{\rm max}$.

We consider next the differential rotation and dynamo for two cases of stellar mass smaller and larger than the Sun. The consideration indicates that equatorial symmetry of the dominant dynamo mode also depends on temperature.

Figures 6–8 visualize the differential rotation, meridional flow and magnetic time-latitude diagram, respectively, computed for a 0.8 $M_\odot$ star. Similar to the Sun, dipolar dynamo mode dominates in this case. The dynamo arrived at dipolar parity from a mixed-parity initial state of Equation (18).

Figures 9–11 display the differential rotation, meridional flow and field diagram computed for a 1.2 $M_\odot$ star. The differential rotation pattern in Figure 9 is similar to that in Figure 6 in spite of about five times faster rotation of the 1.2 $M_\odot$ star. This result contrasts with the dependence of differential rotation on rotation rate produced by our model for fixed stellar mass. The differential rotation changes toward a cylinder-shaped pattern with increasing rotation in a star of given mass. The change results in a weaker meridional flow for faster rotation (see Figures 4 and 5 in Kitchatinov & Olemskoy 2012). The weakening of meridional flow is the probable reason for longer activity cycles in faster rotating stars (of a given mass) found by Jouve et al. (2010) and Karak et al. (2014) with the flux-transport dynamo models. A change toward cylinder-shaped rotation does not happen between Figures 6 and 9 of this paper because these figures correspond to computations for different stellar mass but the same Rossby number of Equation (1). The effect of rotation on large-scale flow is measured by the dimensionless Coriolis number $\Omega^* = 4\pi{\rm Ro}^{-1}$ of Equation (13). The characteristic Coriolis number has the same value of $\Omega^* \simeq 6$ in all computations of this paper. This value is below the range of $10 < \Omega^* < 20$

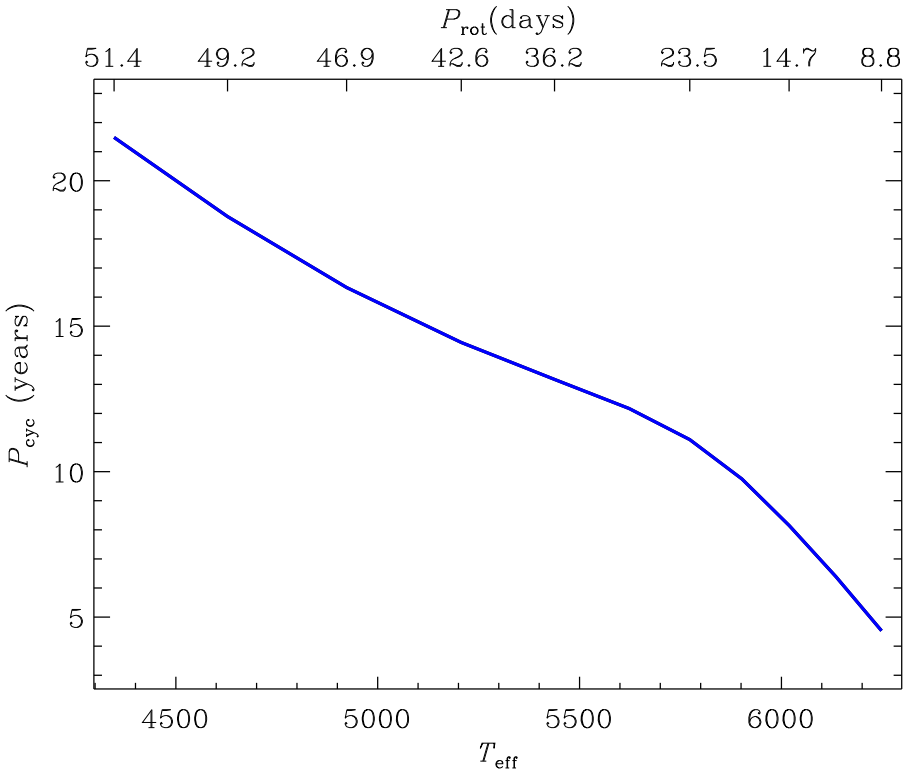

Figure 5. Periods of the computed dynamo-cycles as a function of temperature. Similar to Figure 4, the scale on the top shows the corresponding rotation period.

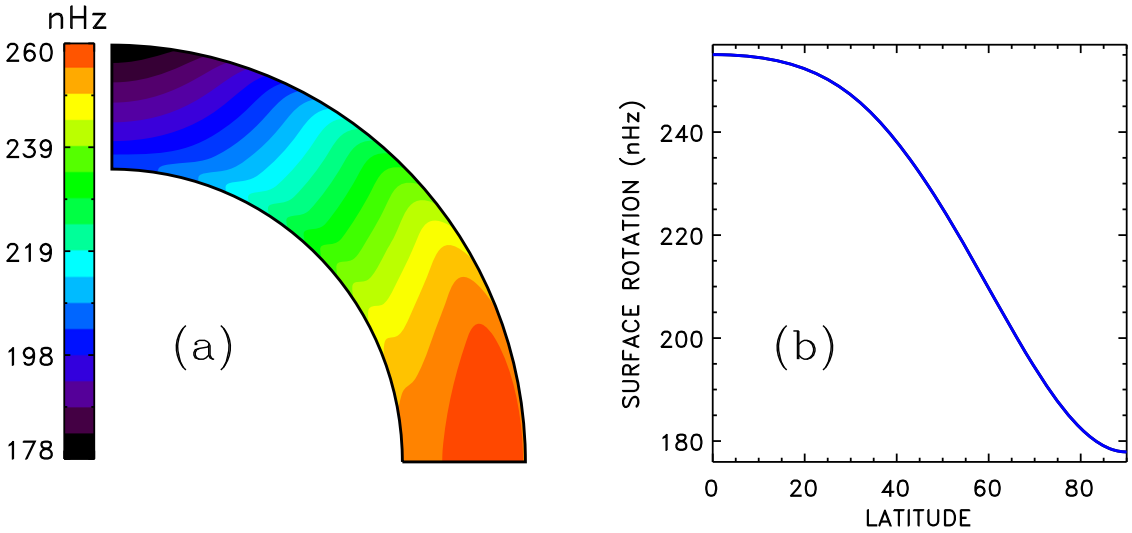

Figure 6. Differential rotation of a 0.8 $M_\odot$ star. (a) Rotation rate isolines in the NW quadrant of the meridional cross-section of the convection zone. (b) Latitudinal profile of the surface rotation rate.

where the change to cylinder-shaped rotation occurs (Kitchatinov & Olemskoy 2012). Deviation from cylinder-shaped rotation is caused by a slight increase of the mean temperature with latitude in the convection zone. The differential temperature results in our model from the rotationally induced anisotropy of the eddy heat transport (Rüdiger et al. 2005). The anisotropy is controlled by the Coriolis number of Equation (13). Computations for different stellar mass and rotation rate but the same characteristic value of Ω^* give similarly shaped differential rotation.

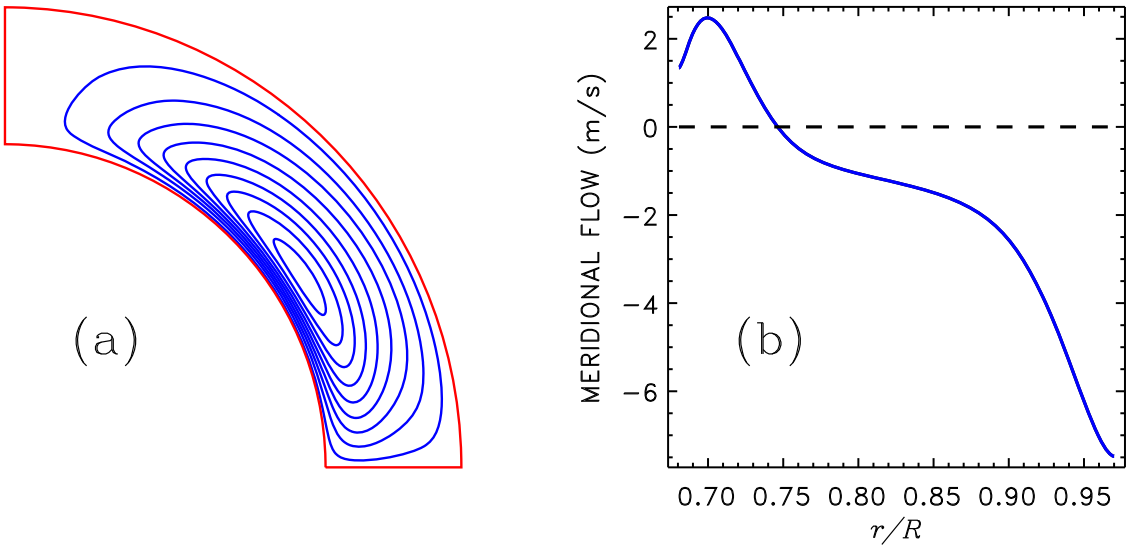

Figure 7. Meridional flow in the 0.8 $M_\odot$ star. (a) Stream lines of the flow. (b) Variation of the meridional velocity with radius at the 45° latitude. Positive velocity means equator-ward flow.

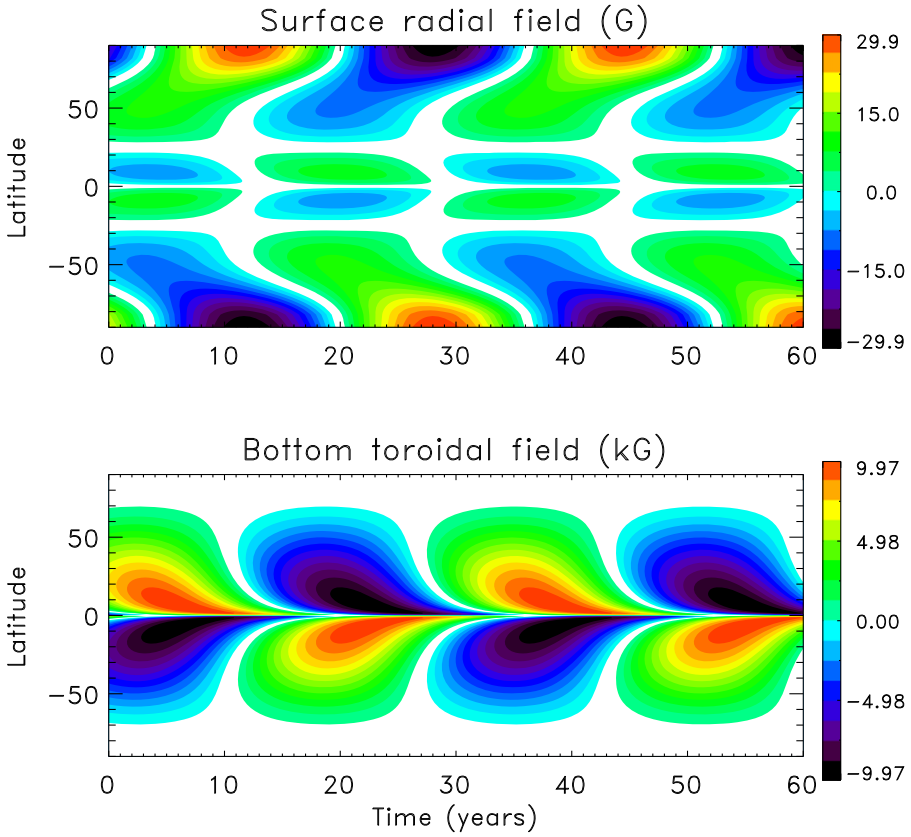

Figure 8. Time-latitude diagrams of the dynamo model for the 0.8 $M_\odot$ star. Surface radial field and the bottom toroidal field are depicted in the top and bottom panels respectively.

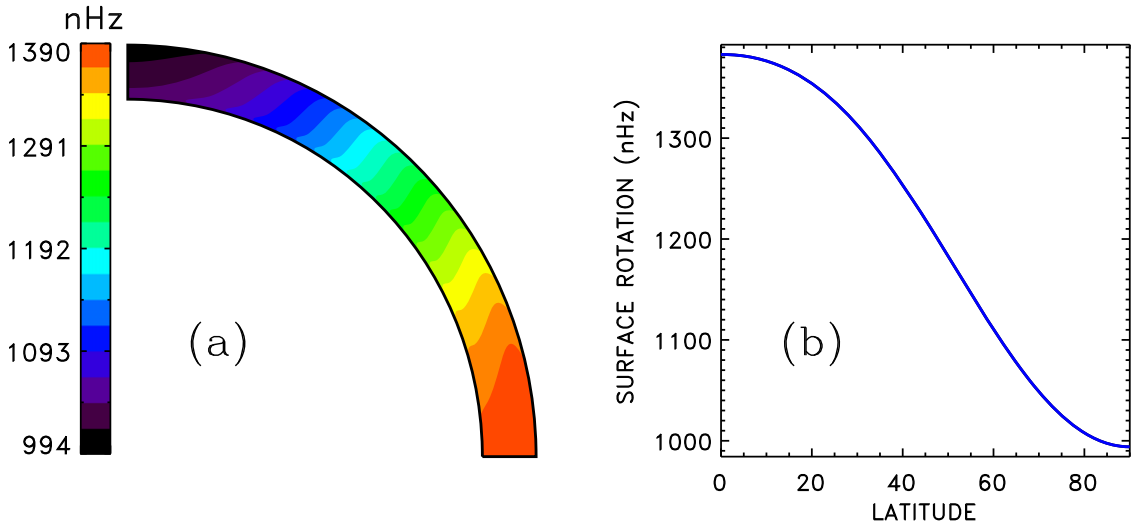

Figure 9. Differential rotation of the 1.2 $M_\odot$ star. (a) Rotation rate isolines. (b) Latitudinal profile of the surface rotation rate.

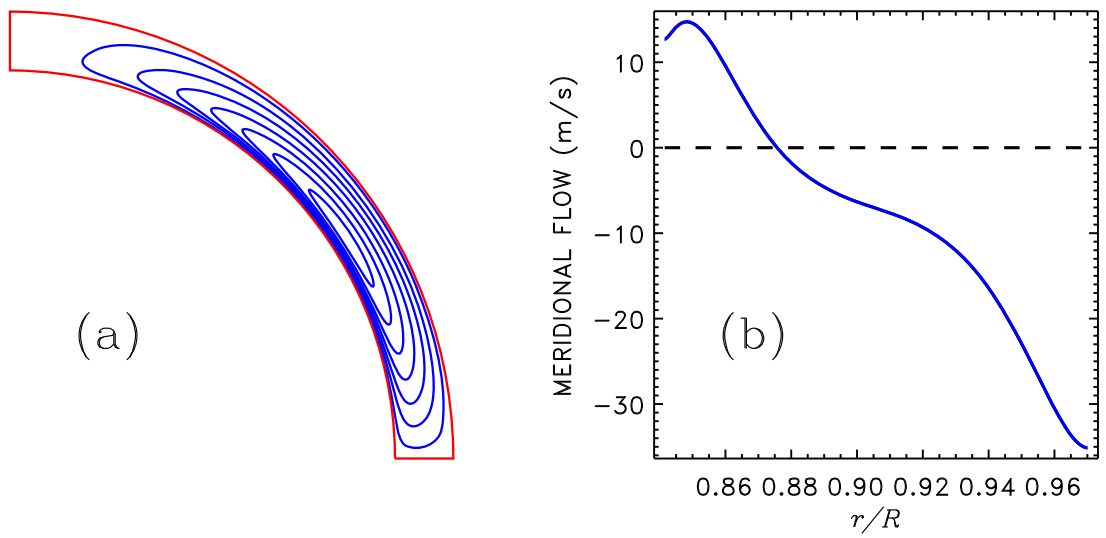

Figure 10. Meridional flow in the 1.2 $M_\odot$ star. (a) Stream lines of the flow. (b) Depth profile of the meridional velocity at the 45° latitude. Positive velocity means equator-ward flow.

Computations for the 1.2 $M_\odot$ star show dynamo convergence to the mixed parity solution. The field diagram in Figure 11 displays mixed equatorial symmetry. Convergence to a certain symmetry requires a certain link between the northern and southern hemispheres. The hemispheric link weakens with decreasing thickness of the convection zone in stars with larger mass.

Another manifestation of the weaker hemispheric link in the thin convection zones is the almost equal threshold amplitudes α_c^d and α_c^q for generation of dipolar and quadrupolar fields in Figure 12. The α_c for this figure increases with temperature. A larger α_c needs faster rotation. This can explain the shorter P_{max} for more massive stars (smaller $B-V$) in Figure 1. The spindown is caused by the large-scale magnetic fields increasing the co-rotation radius for the stellar wind plasma. The spindown stops when rotation slows to relatively large rate corresponding to the relatively large α_c in more massive stars. Further increase in α_c for $M > 1.2\ M_\odot$ may eventually mean that even $P_{rot} \sim 1$ day of *ZAMS* stars does not suffice for a dynamo. Based on observations, Durney & Latour (1978) concluded that stars with spectral type earlier than F6 do not support large-scale dynamos.

The α-effect in our computations is 10% supercritical, $\alpha = 1.1\ \alpha_c$. Computations with other slightly supercritical α

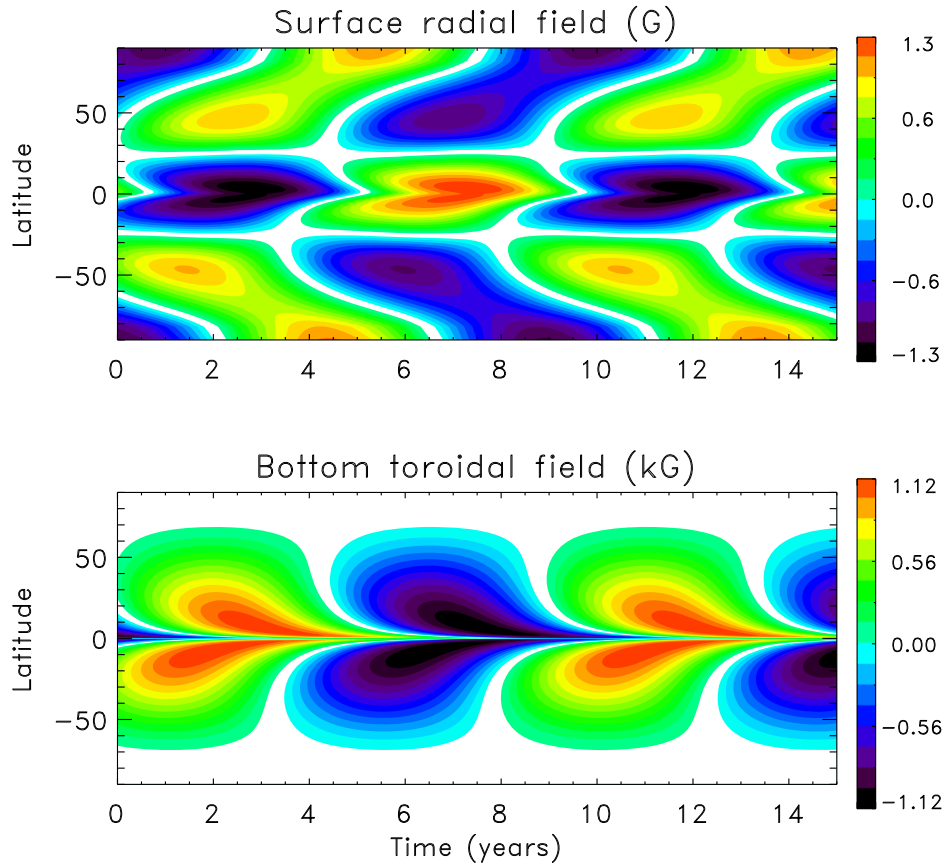

Figure 11. Time-latitude diagrams of the dynamo model for the 1.2 $M_\odot$ star. Surface radial field and bottom toroidal field are displayed in the top and bottom panels respectively.

show that the amplitude B of magnetic cycles is proportional to the square root of the super-criticality, $B \propto (\alpha - \alpha_c)^{1/2}$. This relation holds not only for the dynamo-instability, but is a general rule for any weakly nonlinear instability (see Equation (26.10) in Landau & Lifshitz 1987). The relation can be reformulated in terms of the rotation rate,

$$B \propto (P_{\rm max} - P_{\rm rot})^{1/2}\,, \qquad (21)$$

and possibly explain why the Sun is observed to be less active than other stars with comparable effective temperature and rotation rate (Zhang et al. 2020; Reinhold et al. 2020). According to Equation (21), what matters for magnetic activity is not the value of the rotation rate but the amount of excess of the rate above its marginal value for dynamo. The derivative of Equation (21) on $P_{\rm rot}$ is infinite at $P_{\rm rot} = P_{\rm max}$. Stars with close rotation rates can differ considerably in super-criticality of their dynamos and therefore in the level of magnetic activity.

The ratio of the cycle period to the time of advection by the meridional flow, $P_{\rm cyc}V_{\rm bot}/r_{\rm i}$, varies little and remains between the values of 3 and 4 in our computations; $V_{\rm bot}$ is the near-bottom maximum value of the meridional flow velocity (see Figures 7(b) and 10(b)). This means that the computations belong to the flux-transport dynamo regime. Faster meridional flow in hotter stars explains their shorter cycles.

A preliminary run of one-thousand years starting from the mixed-parity initial state of Equation (18) did not converge to a certain equatorial symmetry for the 1.2 $M_\odot$ star though $\alpha_c^{\rm q}$ is slightly smaller than $\alpha_c^{\rm d}$ in this case (Figure 11). We did not extend the run further for the following reason. Our computations do not include fluctuations in dynamo parameters, which are most probably present in stars. The equator-asymmetric fluctuations couple the dipolar and quadrupolar dynamo modes so that the amplitudes of these modes vary irregularly on a timescale comparable to the cycle period (Schüssler & Cameron 2018; Kitchatinov & Khlystova 2021). The amplitudes are expected to be comparable for almost equal super-criticality of the two modes. This will result in irregularly varying north–south asymmetry in activity of a star. Observational detection of an activity cycle may be difficult in this case if the inclination angle of the rotation axis is not close to $\pi/2$. This may be the reason for no detections of high-quality cycles for stars hotter than the Sun (Figure 1).

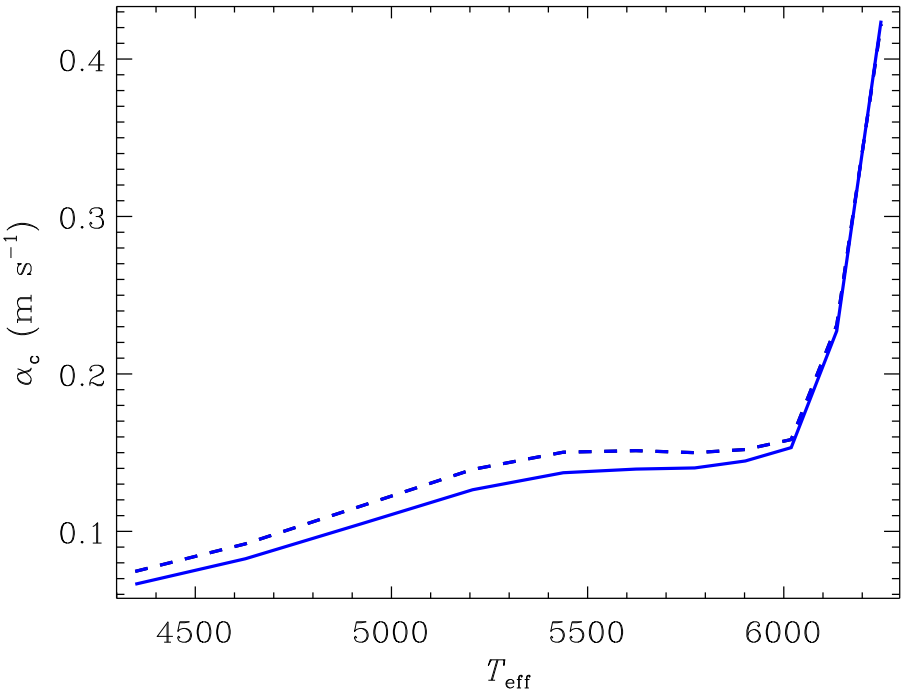

Figure 12. Marginal amplitude α_c of the α-effect for generation of dipolar (solid line) and quadrupolar (dashed line) magnetic fields as a function of temperature.

5. Conclusions

Young rapidly rotating stars are not likely to exhibit Sun-like activity cycles. Otherwise, the large-scale stellar dynamos would be an exception among other hydromagnetic instabilities manifesting turbulence rather than cyclic overstability in a highly supercritical regime.

The upper bound on the rotation period of main sequence dwarfs showing solar-type magnetic activity (Rengarajan 1984; Metcalfe et al. 2016; van Saders et al. 2016) can be interpreted as the minimum rotation rate for large-scale stellar dynamos. This rotation rate increases with the effective temperature. Computations with a joint model for differential rotation and dynamo show magnetic cycles for slightly supercritical dynamos in stars with different mass. Hotter stars have shorter cycles in the computations and the hotter stars rotate faster. The observed decrease in cycle duration for faster rotation based on combined statistics of stars with different spectral types can, therefore, be at least partly explained by the cycle dependence on temperature.

The computations also yield larger marginal values of the α-effect for dynamo operation in hotter stars. A larger α demands faster rotation. This may be the reason for the smaller upper bound on the rotation period for hotter stars. The amplitude of magnetic energy in the dynamo model is proportional to the difference between rotation rate and the marginal rate for dynamo (see Equation (21)). Stars with similar rotation rates can therefore differ substantially in level of their activity as observed (Reinhold et al. 2020): a small difference in rotation rate does not necessarily mean an equally small difference in the super-criticality.

Large variations in differential rotation and cycle period computed for the constant Rossby number of Equation (1) indicate that this number may not be the universal scaling parameter for stellar rotation and dynamos. The Rossby number measures intensity of interaction between convection and rotation. It can be doubted that the BL-mechanism of the solar-type dynamos is fully controlled by this interaction.

The dynamo computations predict a change in equatorial symmetry of global magnetic fields with temperature. The stars with solar and smaller mass show antisymmetric fields about the equator in the computations. A change to mixed-parity asymmetric fields is predicted for more massive stars. The mixed-parity dynamos can impede observational detection of the activity cycles.

The well-defined activity cycle of subgiant HD 81809 is very interesting and challenging to dynamo theory (see the footnote 1). This star exceeds the Sun in mass $M = (1.70 \pm 0.64)\ M_\odot$ (see Table 2 in Egeland 2018). A main sequence A-star is its probable progenitor. A-stars do not have (sufficiently thick) external convection zones and do not show activity cycles. The convection zone formed when HD 81809 evolved from the main sequence is probably responsible for its cyclic activity. This example can be informative on the role of convective envelopes for stellar dynamos.

Acknowledgments

The author is thankful to an anonymous referee for pertinent and constructive comments and to Maria Katsova for a useful discussion. This work was financially supported by the Ministry of Science and High Education of the Russian Federation.

References

Baliunas, S. L., Donahue, R. A., Soon, W. H., et al. 1995, ApJ, 438, 269
Balona, L. A., & Abedigamba, O. P. 2016, MNRAS, 461, 497
Barnes, J. R., Collier Cameron, A., Donati, J. F., et al. 2005, MNRAS, 357, L1
Barnes, S. A. 2007, ApJ, 669, 1167
Böhm-Vitense, E. 2007, ApJ, 657, 486
Boro Saikia, S., Marvin, C. J., Jeffers, S. V., et al. 2018, A&A, 616, A108
Brandenburg, A., Saar, S. H., & Turpin, C. R. 1998, ApJL, 498, L51
Brun, A. S., Strugarek, A., Noraz, Q., et al. 2022, ApJ, 926, 21
Cameron, R. H., & Schüssler, M. 2016, A&A, 591, A46
Cameron, R. H., & Schüssler, M. 2017, ApJ, 843, 111
Chandrasekhar, S. 1961, Hydrodynamic and Hydromagnetic Stability (Oxford: Clarendon)
Charbonneau, P. 2020, LRSP, 17, 4
Choudhuri, A. R., Schussler, M., & Dikpati, M. 1995, A&A, 303, L29
Collier Cameron, A., & Donati, J. F. 2002, MNRAS, 329, L23
Donahue, R. A., Saar, S. H., & Baliunas, S. L. 1996, ApJ, 466, 384
Donati, J. F., & Collier Cameron, A. 1997, MNRAS, 291, 1
D'Silva, S., & Choudhuri, A. R. 1993, A&A, 272, 621
Durney, B. R. 1995, SoPh, 160, 213
Durney, B. R., & Latour, J. 1978, GApFD, 9, 241
Egeland, R. 2018, ApJ, 866, 80
Guerrero, G., & de Gouveia Dal Pino, E. M. 2008, A&A, 485, 267
Hazra, G., Jiang, J., Karak, B. B., & Kitchatinov, L. 2019, ApJ, 884, 35
Høg, E., Fabricius, C., Makarov, V. V., et al. 2000, A&A, 355, L27
Jermyn, A. S., Lesaffre, P., Tout, C. A., & Chitre, S. M. 2018, MNRAS, 476, 646
Jiang, J., Cameron, R. H., Schmitt, D., & Işık, E. 2013, A&A, 553, A128
Jouve, L., Brown, B. P., & Brun, A. S. 2010, A&A, 509, A32
Karak, B. B., & Cameron, R. 2016, ApJ, 832, 94
Karak, B. B., Kitchatinov, L. L., & Choudhuri, A. R. 2014, ApJ, 791, 59
Katsova, M. M., Bondar, N. I., & Livshits, M. A. 2015, ARep, 59, 726
Kitchatinov, L., & Khlystova, A. 2021, ApJ, 919, 36
Kitchatinov, L., & Nepomnyashchikh, A. 2017b, MNRAS, 470, 3124
Kitchatinov, L. L. 2020, ApJ, 893, 131
Kitchatinov, L. L., & Nepomnyashchikh, A. A. 2016, AdSpR, 58, 1554
Kitchatinov, L. L., & Nepomnyashchikh, A. A. 2017a, AstL, 43, 332
Kitchatinov, L. L., & Olemskoy, S. V. 2011, MNRAS, 411, 1059
Kitchatinov, L. L., & Olemskoy, S. V. 2012, MNRAS, 423, 3344
Kitchatinov, L. L., Pipin, V. V., & Rüdiger, G. 1994, AN, 315, 157
Kitchatinov, L. L., & Rüdiger, G. 1999, A&A, 344, 911
Kraft, R. P. 1967, ApJ, 150, 551
Krause, F., & Rädler, K. H. 1980, Mean-field Magnetohydrodynamics and Dynamo Theory (Oxford: Pergamon)
Landau, L. D., & Lifshitz, E. M. 1987, Fluid Mechanics. Vol.6 of Course of Theoretical Physics (Oxford: Pergamon)
Metcalfe, T. S., & Egeland, R. 2019, ApJ, 871, 39
Metcalfe, T. S., Egeland, R., & van Saders, J. 2016, ApJL, 826, L2
Noyes, R. W., Hartmann, L. W., Baliunas, S. L., Duncan, D. K., & Vaughan, A. H. 1984a, ApJ, 279, 763
Noyes, R. W., Weiss, N. O., & Vaughan, A. H. 1984b, ApJ, 287, 769
Olspert, N., Lehtinen, J. J., Käpylä, M. J., Pelt, J., & Grigorievskiy, A. 2018, A&A, 619, A6
Paxton, B. 2004, PASP, 116, 699
Pipin, V. V. 2008, GApFD, 102, 21
Pipin, V. V. 2021, MNRAS, 502, 2565
Pipin, V. V., Sokoloff, D. D., & Usoskin, I. G. 2012, A&A, 542, A26
Reinhold, T., Shapiro, A. I., Solanki, S. K., et al. 2020, Sci, 368, 518
Rengarajan, T. N. 1984, ApJL, 283, L63
Rüdiger, G., Egorov, P., Kitchatinov, L. L., & Küker, M. 2005, A&A, 431, 345
Rüdiger, G., Kitchatinov, L. L., & Hollerbach, R. 2013, Magnetic Processes in Astrophysics: Theory, Simulations, Experiments (Weinheim: Wiley)
Saar, S. H., & Brandenburg, A. 1999, ApJ, 524, 295
Schüssler, M., & Cameron, R. H. 2018, A&A, 618, A89
Skumanich, A. 1972, ApJ, 171, 565
Strugarek, A., Beaudoin, P., Charbonneau, P., & Brun, A. S. 2018, ApJ, 863, 35
Strugarek, A., Beaudoin, P., Charbonneau, P., Brun, A. S., & do Nascimento, J. D. 2017, Sci, 357, 185
van Saders, J. L., Ceillier, T., Metcalfe, T. S., et al. 2016, Natur, 529, 181
van Saders, J. L., Pinsonneault, M. H., & Barbieri, M. 2019, ApJ, 872, 128
VandenBerg, D. A., & Clem, J. L. 2003, AJ, 126, 778
Warnecke, J. 2018, A&A, 616, A72
Wilson, O. C. 1978, ApJ, 226, 379
Zhang, J., Shapiro, A. I., Bi, S., et al. 2020, ApJL, 894, L11
Zhang, Z., & Jiang, J. 2022, ApJ, 930, 30